View metadata, citation and similar papers at core.ac.uk

brought to you by CORE

provided by Open Repository and Bibliography - Luxembourg

Absorption Coefficient of a Semiconductor Thin Film from Photoluminescence

G. Rey,[*] C. Spindler, F. Babbe, W. Rachad, and S. Siebentritt

Laboratory for Photovoltaics, Physics and Materials Science Research Unit, L-4422 Belvaux, Luxembourg

M. Nuys and R. Carius

Forschungszentrum Jülich GmbH Institut für Energie und Klimaforschung, 52425 Jülich, Germany

S. Li and C. Platzer-Björkman

Ångström Solar Center, Solid State Electronics, Uppsala University, 751 21 Uppsala, Sweden

(Received 10 May 2017; revised manuscript received 8 February 2018; published 8 June 2018)

The photoluminescence (PL) of semiconductors can be used to determine their absorption coefficient (α) using Planck's generalized law. The standard method, suitable only for self-supported thick samples, like wafers, is extended to multilayer thin films by means of the transfer-matrix method to include the effect of the substrate and optional front layers. α values measured on various thin-film solar-cell absorbers by both PL and photothermal deflection spectroscopy (PDS) show good agreement. PL measurements are extremely sensitive to the semiconductor absorption and allow us to advantageously circumvent parasitic absorption from the substrate; thus, α can be accurately determined down to very low values, allowing us to investigate deep band tails with a higher dynamic range than in any other method, including spectrophotometry and PDS.

DOI: 10.1103/PhysRevApplied.9.064008

I. INTRODUCTION

Sub-band-gap absorption in semiconductors is a critical parameter for device application because sub-band-gap absorption is due to defects and disorder, which influence the performance of any semiconductor-based device [1]. Thin-film transistors are good examples: the mobility is affected by band tailing [2], although the band-tail-state effect on carrier transport is strongly material dependent [3]. Band tails are also known to reduce the efficiency of solar cells [4,5] and to be the limiting factor in the case of amorphous Si solar cells [6].

Recently, De Wolf *et al.* showed an empirical linear relationship between band tailing and the voltage deficit (the difference between band-gap energy and open-circuit voltage) for several solar-cell technologies [7]. Band tailing in semiconductors may occur at both conduction and valence band edges in a nonsymmetrical way [8]. If the band tails are described by Urbach behavior [9] [exponential decrease of the density of states (DOS) from the band edges towards midgap], which is observed in most materials [10–14], the extension of the joint DOS below the band-gap energy is determined by the band edge, which shows the broadest extension into the band gap [15].

Besides Urbach behavior, various models have been proposed to describe nonexponential tails [16]. As the joint DOS is reflected in the absorption coefficient, α, its measure in the sub-band-gap energy region is of prime interest for band-tail investigations. Because the sub-band-gap absorbance is weak, especially for thin films, photoluminescence (PL) can be advantageously used due to its capability of measuring extremely low α values, whereas other methods such as ellipsometry and spectrophotometry are limited.

Indeed, PL has been proven to be able to measure α down to 10^{-16} cm^{-1} on Si wafers [17]. The equation rigorously derived for self-supporting samples like wafers has also been applied to thin films [16]. But in that case, the difference between the front interface, the film-substrate interface, and the substrate back-side reflectivity is ignored. Here, we propose a rigorous yet analytical method to retrieve α from PL spectra measured on multilayered structures. We also discuss the advantages and limitations of PL-based absorption measurements in the case of defect-related absorption.

II. MODEL

A. Emission and absorption rates

The radiative transition rate per volume and per energy unit between an upper (u) and a lower (l) electronic state can be derived from Fermi's golden rule [18]:

[*]germrey@gmail.com

Published by the American Physical Society under the terms of the Creative Commons Attribution 4.0 International license. Further distribution of this work must maintain attribution to the author(s) and the published article's title, journal citation, and DOI.

$$R_{\rm sa} = \frac{2\pi}{\hbar}\sum_{E_u,E_l}\overline{|\mathcal{H}|^2}\rho_\gamma f_\gamma (n_u n'_l - n'_u n_l)\delta(E_{ul}-\hbar\omega), \quad (1)$$

$$R_{\rm sp} = \frac{2\pi}{\hbar}\sum_{E_u,E_l}\overline{|\mathcal{H}|^2}\rho_\gamma (n_u n'_l)\delta(E_{ul}-\hbar\omega), \quad (2)$$

with $R_{\rm sa}$ being the difference between the stimulated emission rate and the absorption rate and $R_{\rm sp}$ the spontaneous emission rate. The upper and lower states can be the conduction and the valence band, but the considerations are generally valid for any two-state system. E is the energy of the electronic states ($E_{ul} = E_u - E_l$), and $\hbar\omega$ is the photon energy. $\overline{|\mathcal{H}|^2}$ is the square of the matrix element for the interaction between the upper and lower electronic states. Here, the value is averaged over degenerate states. ρ_γ is the photon mode density and f_γ is the photon distribution function, which is given by a Bose-Einstein distribution only if the material is not excited, i.e., there is no luminescence. The density of photons is given by $n_\gamma = \rho_\gamma f_\gamma$. $n_{u,l}$ and $n'_{u,l}$ are the densities of occupied and unoccupied electron states, respectively. Those two quantities can be described as $n_{u,l} = \rho_{u,l} f_{u,l}$ and $n'_{u,l} = \rho_{u,l} f'_{u,l}$, where $\rho_{u,l}$ is the electronic density of states (the degeneracy factor is implicitly included in ρ, even though this factor might differ for n and n'; see the monovalent impurities case in the Appendix), f is the electron distribution, and $f' = 1 - f$. Assuming that the electrons are in thermal equilibrium with each other, the electron distributions reduce to Fermi-Dirac distributions, with a quasi-Fermi level $\mu_{u,l}$.

The absorption coefficient α can be defined as the power absorbed per unit volume divided by the incident energy flux, which translates into Beer's absorption law, in one dimension:

$$d\Phi/dx = -\alpha\Phi, \quad (3)$$

where both sides of the equation are divided by $\hbar\omega$ to replace the light intensity by the photon flux Φ. To describe the flux of photons within the material, we use the continuity equation. Since photons can be absorbed or emitted, the net generation rate is given by the difference between the rates for emission and absorption. To derive α, we first consider the case without spontaneous emission. Then the generation rate, $R_{\rm sa}$, is given by the difference between the stimulated emission rate and the absorption rate given in Eq. (1):

$$\vec{\nabla}\cdot\vec{\Phi} + \frac{\partial n_\gamma}{\partial t} = R_{\rm sa}, \quad (4)$$

which reduces to $d\Phi/dx = R_{\rm sa}$ for the steady-state and one-dimensional cases, corresponding to a material without lateral variation of carrier densities (i.e., the excitation spot size must be larger than the carrier diffusion length). Since, in Eq. (1), $\rho_\gamma f_\gamma = n_\gamma = v_\gamma^{-1}\Phi$, with v_γ being the photon velocity, the absorption coefficient can be derived as

$$\alpha = \frac{2\pi}{\hbar} v_\gamma^{-1}\sum_{E_u,E_l}\overline{|\mathcal{H}|^2}(n'_u n_l - n_u n'_l)\delta(E_{ul}-\hbar\omega). \quad (5)$$

To describe the upper and lower densities, we consider transitions involving bands or monovalent defects; the ratio

$$\frac{n_u n'_l}{n'_u n_l - n_u n'_l} = \frac{1}{\exp(\frac{\hbar\omega-\Delta\mu}{k_B T}) - 1} \quad (6)$$

depends not on E_u or E_l (see the Appendix for the derivation) but on $\Delta\mu$, the quasi–Fermi-level splitting (QFLS). Thus, this ratio can be removed from the sum in Eq. (2), leading to the equivalent of the van Roosbroeck–Shockley equation [19], modified to include the nonequilibrium condition, which is described by the QFLS [20]:

$$R_{\rm sp} = \alpha\frac{v_\gamma\rho_\gamma}{\exp(\frac{\hbar\omega-\Delta\mu}{k_B T}) - 1} = \alpha\Gamma. \quad (7)$$

B. Light propagation

Now, considering spontaneous emission with a rate $R_{\rm sp}$, given in Eq. (2), in addition to $R_{\rm sa}$, the photon continuity equation becomes [17]

$$\vec{\nabla}\cdot\vec{\Phi} = R_{\rm sp} + R_{\rm sa} = \alpha\Gamma - \alpha\Phi. \quad (8)$$

A useful case for photoluminescence analysis is when $\Delta\mu$ and α can both be assumed to be constant throughout the luminescent film. The position-dependent $\Delta\mu$ case can be treated numerically or by integration over the thickness if the spatial variation is known [21,22]. Constant $\Delta\mu$ and α correspond to a homogeneous semiconductor film with good transport properties. Assuming planar geometry for the semiconductor film, we can restrain the derivation to one dimension with the position given by the x coordinate, as depicted in Fig. 1. The photon flux traveling towards positive x, Φ^+, and the photon flux traveling towards negative x, Φ^-, are the one-dimensional solutions of Eq. (8):

$$\Phi^\pm(x) = \Gamma + C^\pm\exp(\mp\alpha x), \quad (9)$$

with the constants $C^\pm$ depending on the boundary conditions.

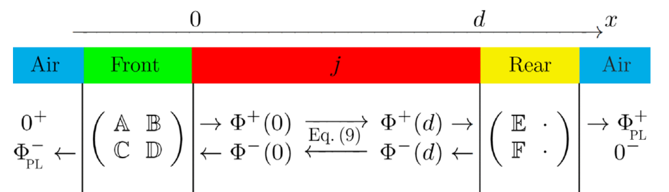

FIG. 1. Diagram of the optical system with photon fluxes.

An elegant way to impose the boundary conditions is to use the transfer-matrix method. Here, we restrain our analysis to films which show weak or no interference fringes in their transmittance or reflectance spectra due to significant thickness or surface roughness, as is often seen for polycrystalline absorbers of thin-film solar cells. The intensity matrix, which gives directly the relationship between light intensities, should be used in such a case [23]. One may use field matrices to treat coherent light propagation. As shown in Fig. 1, the optical system representing the sample consists of the following elements.

(a) Front: a front part that is described by the intensity matrix coefficients $\mathbb{A}$, $\mathbb{B}$, $\mathbb{C}$, and $\mathbb{D}$. This front part can account for additional top layers, if there are any, and their associated interfaces. For the simplest system, the front part describes only the air-film interface. The front matrix then reduces to [23]

$$\begin{pmatrix} \mathbb{A} & \mathbb{B} \\ \mathbb{C} & \mathbb{D} \end{pmatrix}_{0|j} = \frac{n_0/n_j}{|t_{0j}|^2} \begin{pmatrix} 1 & -|r_{j0}|^2 \\ |r_{0j}|^2 & |t_{0j}t_{j0}|^2 - |r_{0j}r_{j0}|^2 \end{pmatrix}, \tag{10}$$

with t and r being the Fresnel coefficients, for normal incidence $t_{ab} = 2\tilde{n}_a/(\tilde{n}_a + \tilde{n}_b)$ and $r_{ab} = (\tilde{n}_a - \tilde{n}_b)/(\tilde{n}_a + \tilde{n}_b)$, with $\tilde{n} = n + ik$ being the complex refractive index. Subscript 0 refers to the air and subscript j refers to the luminescent layer.

(b) j: the luminescent layer of thickness d in which the light propagation is governed by Eq. (9).

(c) Rear: a rear part that can account for interface effects, and an optional substrate which is described by $\mathbb{E}$ and $\mathbb{F}$. Since no light is entering the optical system from the back side of the substrate, the right part of this matrix is of no influence.

The boundary conditions are then directly given by

$$\begin{pmatrix} 0 \\ \Phi_{\mathrm{PL}}^- \end{pmatrix} = \begin{pmatrix} \mathbb{A} & \mathbb{B} \\ \mathbb{C} & \mathbb{D} \end{pmatrix} \begin{pmatrix} \Phi^+(0) \\ \Phi^-(0) \end{pmatrix}, \tag{11}$$

$$\begin{pmatrix} \Phi^+(d) \\ \Phi^-(d) \end{pmatrix} = \begin{pmatrix} \mathbb{E} & \cdot \\ \mathbb{F} & \cdot \end{pmatrix} \begin{pmatrix} \Phi_{\mathrm{PL}}^+ \\ 0 \end{pmatrix}. \tag{12}$$

Φ_{PL}^- and Φ_{PL}^+ are the PL fluxes emitted at the front and at the back surface of the stacked sample, respectively. It should be stressed that PL is the photoemission additional to the thermal dark (gray-body) emission. Thus, there are no incoming fluxes considered in Eqs. (11) and (12) since the dark photon flux has zero divergence and is treated as a constant background, assuming that the sample is in thermal equilibrium with its surrounding environment. For exactness, according to the previous PL definition, the dark emission contribution to R_{sp} with $\Delta\mu = 0$ should be removed, but, for PL measurements, $\{\exp[(\hbar\omega - \Delta\mu)/k_B T] - 1\}^{-1} \gg [\exp(\hbar\omega/k_B T) - 1]^{-1}$, and such a correction is disregarded.

By use of Eqs. (9), (11), and (12), the emitted PL flux at the front can be expressed as

$$\Phi_{\mathrm{PL}}^- = \Gamma \frac{(\mathbb{D} - \frac{\mathbb{B}}{\mathbb{A}}\mathbb{C})(1 - e^{-\alpha d})(1 + \frac{\mathbb{F}}{\mathbb{E}} e^{-\alpha d})}{1 + \frac{\mathbb{F}}{\mathbb{E}}\frac{\mathbb{B}}{\mathbb{A}} e^{-2\alpha d}} = \Gamma\Theta, \tag{13}$$

which is simply the product of Γ, the blackbody spectrum modified by the QFLS, and Θ, an optical correction factor which takes into account that the light emitted inside the luminescent material has to escape from the sample to be detected as a PL signal, but which also includes how the light intensity increases when light is propagating through the layer thickness. From the transfer-matrix method, it can be shown that the optical factor Θ is the absorptivity of the layer j.

Equation (13) gives the PL flux generalized to a multilayer system. For a wafer, $\mathbb{B}/\mathbb{A} = -|r_{j0}|^2$, $\mathbb{D} - (\mathbb{B}/\mathbb{A})\mathbb{C} = 1 - |r_{j0}|^2$, and $\mathbb{F}/\mathbb{E} = |r_{j0}|^2$, and the PL emission given by Eq. (13) reduces to the equation reported by Daub and Würfel [17] when considering homogeneous $\Delta\mu$ and α values throughout the film thickness. If the wafer has different front-side and back-side reflectivity, Eq. (13) reduces to the expression reported in Refs. [24,25].

C. QFLS and absorption coefficient measurement

For a quantitative analysis, we explicitly write the density of the photon mode for both polarizations, neglecting the dispersion of n, $\rho_\gamma = (\Omega_j/4\pi)n_j^3(\hbar\omega)^2(\pi^2\hbar^3c^3)^{-1}$, where c is the vacuum speed of light ($v_\gamma = n_j c$). Ω_j is the solid angle of the light cone that corresponds to the light that can be extracted at the front surface. For the collection of the PL signal into the hemisphere of 2πsr in front of the sample, the corresponding solid angle inside the material is $\Omega_j = 2\pi\{1 - \cos[\sin^{-1}(1/n_j)]\}$, which reduces to π/n_j^2 for large n_j values, as are typically observed for semiconductors in the visible and near-infrared range.

Following the approach described in Ref. [26], prior to the evaluation of α, the QFLS must be determined, which can be done by rewriting Eqs. (7) and (13) as

$$\frac{\hbar\omega - \Delta\mu}{k_B T} = \ln\left[\frac{n_j^2\Omega_j(\hbar\omega)^2}{4\pi^3\hbar^3c^2}\frac{\Theta}{\Phi_{\mathrm{PL}}^-} + 1\right]. \tag{14}$$

Besides the measurement of the PL signal, the determination of $\Delta\mu$ and $k_B T$ requires the knowledge of Θ. This term is obtained from the complex refractive index measured by another technique, such as spectrophotometry (SP) or spectroscopic ellipsometry (SE), which is reliable in the high- and midabsorption range. Provided that Θ is known, PL data can be linearly fitted using Eq. (14) to retrieve $\Delta\mu$ and $k_B T$. Note that $\Delta\mu$ and T are not wavelength dependent, and therefore it is sufficient to determine the complex refractive index over only a narrow spectral range to apply the method prior to PL data evaluation. The

range where the complex refractive index has to be measured by a complementary technique corresponds typically to the highest energy range of the PL signal, while the low-energy PL signal is used to accurately determine α in the low-absorbing range. Once $\Delta\mu$ and T are determined, one may extract α by using Eq. (13):

$$\alpha = -\frac{1}{d}\ln\left(\frac{(\frac{\mathbb{F}}{\mathbb{E}}-1)+\chi}{2\frac{\mathbb{F}}{\mathbb{E}}(1+\frac{\Phi_{PL}^{-}/\Gamma}{(\frac{\mathbb{A}}{\mathbb{B}}\mathbb{D}-\mathbb{C})})}\right), \quad (15)$$

where

$$\chi = \sqrt{\left(\frac{\mathbb{F}}{\mathbb{E}}-1\right)^2 + 4\frac{\mathbb{F}}{\mathbb{E}}\left(1+\frac{\Phi_{PL}^{-}/\Gamma}{(\frac{\mathbb{A}}{\mathbb{B}}\mathbb{D}-\mathbb{C})}\right)\left(1-\frac{\Phi_{PL}^{-}/\Gamma}{(\mathbb{D}-\frac{\mathbb{B}}{\mathbb{A}}\mathbb{C})}\right)}.$$

It must be stressed that in the low absorption range, $n \gg k$ and the Fresnel coefficient depends only weakly on k. Therefore, the optical matrix elements $\mathbb{A},\ldots,\mathbb{F}$, used in Eq. (15), can be calculated from SP or SE data because, contrary to k, n is accurately measured by those techniques, even in the low absorption range. In conclusion, the data evaluation can be summarized as follows: First, n is measured over the full range by a complementary technique (for example, SE or SP) and k is measured in the high energy range of the PL, where the absorption coefficient is high. Then the PL data measured in the high-energy range together with n and k are used to determine $\Delta\mu$ and T. Finally, the absorption coefficient in the low-energy range is accurately determined from the PL data and n. Taking advantage of the high sensitivity of the PL, very low absorption coefficients can be measured reliably.

We would like to point out that the amount of nonradiative recombination has no influence on the α values determined. Any nonradiative recombination reduces that PL yield, and thus the QFLS. Since the QFLS is determined before extracting the α values, this effect is taken care of. Interestingly, when $\exp[(\hbar\omega-\Delta\mu)/k_BT] \gg 1$, which is fulfilled for a wide range of photon energies in the case of a solar-cell absorber, it can be deduced that $\Gamma \propto \exp(\Delta\mu)$ from Eq. (7), and thus $\Phi_{PL}^{-} \propto \exp(\Delta\mu)$ from Eq. (13). As Eq. (15) involves only the ratio Φ_{PL}^{-}/Γ, the PL yield has no influence on the obtained α values, unlike the spectral shape, which has to be measured accurately. Under these conditions, one could use noncalibrated PL spectra. In that case, the $\Delta\mu$ value extracted from Eq. (14) would not represent the QFLS and should only be seen as a scaling factor without physical meaning, but the absorption coefficient derived from Eq. (15) would be correctly evaluated.

III. EXPERIMENTAL DETAILS

The absorption coefficient of different chalcopyrite thin films, $CuInSe_2$ (CIS), $Cu(In,Ga)Se_2$ (CIGS), and $CuGaSe_2$ (CGS), is measured using different techniques. CIS and CIGS films are deposited on soda-lime glass (SLG) and on Mo-coated SLG by single-stage coevaporation of the pure elements in a molecular beam epitaxy system in order to obtain homogeneous composition throughout the film. Their chemical composition is determined by energy-dispersive x-ray spectroscopy. CGS films are grown by metal-organic vapor-phase epitaxy on GaAs substrates.

The complex refractive index of CIS and CIGS samples are measured by SP. Films grown on Mo-coated SLG are mechanically transferred to transparent substrates. The total transmittance at normal incidence $\mathcal{T}$ and the total reflectance at near-normal incidence $\mathcal{R}$ are measured using a UV–visible–near-infrared spectrophotometer equipped with an integrating sphere. The substrate refractive index is evaluated from $\mathcal{T}$ and $\mathcal{R}$ measurements on the bare substrate. The complex refractive index is retrieved by numerically solving

$$\begin{pmatrix} 1 \\ \mathcal{R} \end{pmatrix} = \begin{pmatrix} \mathbb{A} & \mathbb{B} \\ \mathbb{C} & \mathbb{D} \end{pmatrix} \begin{pmatrix} e^{+\alpha d} & 0 \\ 0 & e^{-\alpha d} \end{pmatrix} \begin{pmatrix} \mathbb{E}\mathcal{T} \\ \mathbb{F}\mathcal{T} \end{pmatrix}, \quad (16)$$

where the film thickness is evaluated by cross-section scanning electron microscopy. The $\mathbb{A}$, $\mathbb{B}$, $\mathbb{C}$, and $\mathbb{D}$ coefficients describe the light-intensity transfers at the interface between the air and the thin film. For instance, $\mathbb{A} = [\mathrm{Re}(n_j)|t_{\mathrm{air}\to j}|^2]^{-1}$ and $\mathbb{B} = -\mathbb{A}|r_{j\to\mathrm{air}}|^2$, with t and r being the Fresnel coefficients. $\mathbb{E}$ and $\mathbb{F}$ include the effects of the thin film–substrate interface, the propagation inside the substrate, and the substrate-air interface.

The complex refractive index of CGS is determined by SE measured at 65°, 70°, and 75°. The ellipsometry parameters are fitted using the following stack from bottom to top: GaAs (500 μm), GaAs oxide (3 nm), CGS (555 nm), and a roughness layer (28 nm).

The PL experiments are conducted under continuous red (660 and 671 nm for the CIS and CIGS samples) or green (514.5 nm for the CGS samples) laser excitations set between 1 and 2 $\mathrm{kW\,m^{-2}}$ for the CIS and CIGS samples and varying from 10 to 60 $\mathrm{kW\,m^{-2}}$ for the CGS samples with a beam radius of 1 mm for all measurements. The PL signal is collected by two parabolic mirrors coupled to a monochromator. The signal is recorded by a Si CCD and an (In,Ga)As array. The spectral response of the detection system is corrected with the help of a calibrated halogen lamp. The intensity calibration is performed using a power meter. The calibration coefficient of absolute PL intensity is determined with an accuracy of $\pm 33\%$.

The absorption measurements by photothermal deflection spectroscopy (PDS) are performed using a conventional PDS experimental setup for transversal deflection [27] with additional features: the synchronous measurement of the PDS signal and its phase shift with respect to the excitation, and the measurement of the amplitudes of both the incident and the transmitted light. This setup offers a convenient and reliable way to determine the absorption

coefficient and to distinguish between film and substrate absorption. The sample is illuminated by a spectrally resolved light source. Depending on the incident power and the absorption, the sample temperature changes, resulting in a change of the temperature gradient in the deflection medium (CCl_4) which is in contact with the film surface. The temperature gradient induces a refractive-index gradient in which a laser beam, which is guided parallel to the film surface, is deflected. At low power, the deflection of the beam, measured by a position-sensitive detector, is proportional to the absorbed power in the film. To achieve the required signal-to-noise ratio, the incident monochromatic light is chopped and the PDS signal is measured with the lock-in technique.

IV. RESULTS AND DISCUSSION

We first focus on the case where the PL signal comes from a single transition process by analyzing the CIS and CIGS samples. In the second part of this section, we discuss the case where both band-to-band and band-to-deep-defect-level are present, as in the CGS samples.

A. Single transition process

Here, we assume that each of the upper (and lower) carrier densities involved in the PL process is described by a unique quasi-Fermi level, which corresponds to band-to-band transitions or a transition involving tail states at room temperature. The absolute PL signal of a CIS thin film is plotted in the inset of Fig. 2. Using this spectrum and the optical factor Θ [defined in Eq. (13)] measured from SP (not shown), we determine the QFLS and the temperature using Eq. (14), as shown in Fig. 2, where the values of $\Delta\mu$ and T, obtained by a linear fit, are given in the legend. The fitting range corresponds not to the center of the peak but to its high-energy wing, where the spectrum is the most influenced by the occupation of states given by the Fermi distribution, i.e., where the QFLS has the strongest influence and also where the absorption coefficient is high and the measurement of Θ by SP is reliable. The deviations from the linear behavior are multiple outside of the fitting range. For the high absorption range ($\hbar\omega > 1.1$ eV), the large scattering is attributed to the low PL signal due to low emission intensity and to reabsorption of the emitted light. Additionally, a bending of the plot may occur in the high-energy range if there is a residual background in the PL signal (potentially originating from instrumental noise or interface states or secondary phase inclusions). For the low absorption range ($\hbar\omega < 1.0$ eV), the curve bending results from inaccuracy in Θ because the complex refractive index cannot be reliably measured by SP in the low absorption range (see Fig. 3).

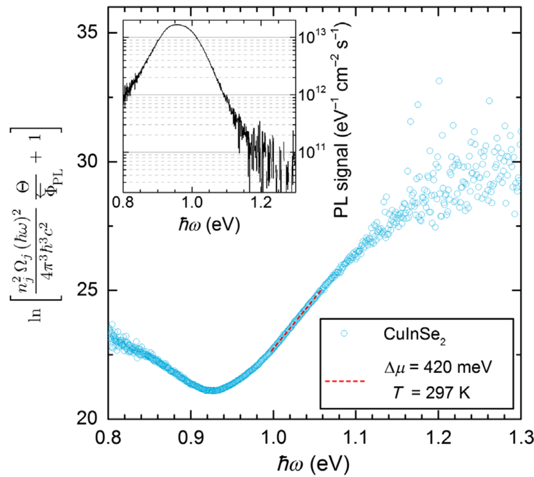

FIG. 2. Determination of $\Delta\mu$ and $k_B T$ from a linear fit in the high-energy range of the PL signal for a $CuInSe_2$ thin film deposited on a soda-lime glass substrate. The optical factor Θ is determined from transmittance and reflectance measurements on the thin film plus substrate and on the bare substrate. (Inset) The corresponding PL spectrum for an emission in the 2π sr in front of the sample.

The α value obtained from Eq. (15) is compared, in Fig. 3, with the SP and PDS measurements. For $\hbar\omega > 1.06$ eV, the PL measurement is limited by the low PL signal, while, for the same range, PDS is not accurate due to signal saturation. SP and PDS have their own limitations to measure small values of α due to internal light trapping for the first one and to the presence of the substrate and small signal for the latter. Within the range of their trustworthiness, the α values measured by the three methods are in good agreement. The PL data (Φ_{PL}^{-}) and the $\Delta\mu$ and $k_B T$ values determined in Fig. 2 are used in Eq. (15) to calculate $\alpha(\mathrm{PL})$. The optical matrix elements $\mathbb{A}, \ldots, \mathbb{F}$ are still derived from a SP measurement. As discussed in Sec. II C, the matrix elements are correctly evaluated as

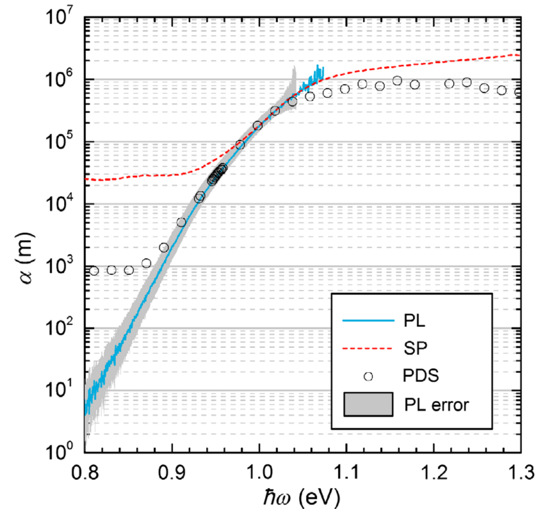

FIG. 3. Comparison of the absorption coefficient of a $CuInSe_2$ thin film deposited on soda-lime glass substrate measured by various methods (PL, photoluminescence; SP, spectrophotometry; PDS, photothermal deflection spectroscopy).

long as k can be accurately measured down to $n \gg k$, where the Fresnel coefficients do not depend on k. SP provides accurate values down to $\alpha = 10^5\ \mathrm{m}^{-1}$, at 1 eV, which translates to $k \simeq 10^{-2} \ll n$. Thus, the optical matrix elements $\mathbb{A}, \ldots, \mathbb{F}$ are correctly evaluated from SP even in the low absorption range.

The absorption spectra reported in Fig. 3 illustrate well our interest in using PL to measure the sub-band-gap absorption of semiconductor thin films. The exponential rise of α in the low absorption range corresponding to Urbach behavior is clearly resolved over several orders of magnitude on the PL-based spectrum, therefore allowing accurate determination of the Urbach energy. Urbach energies measured by PL are reported in Table I for a series of $\mathrm{Cu(In,Ga)Se_2}$ thin films with different compositions. Cu-poor samples show larger Urbach energies since the Cu deficiency leads to heavy doping and heavy compensation, which results in band-edge fluctuation and tailing, as observed previously [28]. CIGS shows higher Urbach energies than CIS (with comparable Cu content) because of alloy disorder.

B. Influence of the optical factor

The influence of the optical factor Θ is analyzed in more detail for comparison with expressions found in the literature. For thin-film investigation with a calibrated PL, the spectral variation of Θ is often disregarded by simply setting $\Theta = 1$ in Eq. (13) [26,29–31]. Here, we compare two approximations for Θ from the perspectives of QFLS and absorption coefficient measurement. The first approximation of Θ is its expression derived for bare thick wafers:

$$\Theta_w = \frac{(1 - |r_{j0}|^2)(1 - e^{-\alpha d})}{(1 - |r_{j0}|^2 e^{-\alpha d})}. \qquad (17)$$

Neglecting reflection at the back side, $|r_{j0}|^2 = \mathcal{R}$ in the numerator of Eq. (17), while $|r_{j0}|^2 = 0$ in the denominator of Eq. (17), which leads to a rougher approximation [26],

$$\Theta'_{1-\mathcal{R}} = (1 - \mathcal{R})(1 - e^{-\alpha d}). \qquad (18)$$

In the high absorption range, when $\alpha d \gg 1$,

TABLE I. Composition-dependent Urbach energies measured by PL for $\mathrm{CuInSe_2}$ and $\mathrm{Cu(In,Ga)Se_2}$ thin films.

Sample	[Cu]/([In] + [Ga])	[Ga]/([In] + [Ga])	E_U (meV)
CIS-262	0.83	0	14.6
CIS-277	0.95	0	11.3
CIS-276	1.10	0	9.9
CIGS-105	0.99	0.32	12.0
CIGS-104	1.01	0.34	11.9

$$\lim_{\alpha d \to \infty} \Theta'_{1-\mathcal{R}} = \Theta_{1-\mathcal{R}} = 1 - \mathcal{R}. \qquad (19)$$

From an experimental point of view, this last approximation benefits from the fact that the knowledge of α is not needed prior to PL data (Φ^-_{PL}) evaluation since only $\mathcal{R}$ is required. After T and $\Delta\mu$ evaluation, α might be extracted by solving $\Phi^-_{\mathrm{PL}} = \Gamma\Theta'_{1-\mathcal{R}}$.

In Fig. 4, we compare the results obtained when using Θ [Eq. (13)], Θ_w [Eq. (17)], and $\Theta_{1-\mathcal{R}}$ [Eq. (19)] for a modeled system made of a 2.5-μm-thick CIS on a Mo substrate, which is the typical stack used for high-efficiency solar cells [32]. We also do the comparison for slightly thinner films (1 μm) on Mo and on SLG.

The complex refractive index of SLG is calculated from SP measurements on a bare SLG, while its values for Mo and CIS are taken from Refs. [33,34], respectively. Data from Ref. [34] are measured from SE, which is inherently limited for absorption measurement in the low-energy range. In order to get a realistic PL spectrum, k from Ref. [34] is modified to present Urbach behavior ($E_U = 20$ meV) for $\hbar\omega < 1$ eV [see the dashed lines in Figs. 4(j)–4(l)]. The PL spectrum, calculated using Eq. (13) with $\Delta\mu = 0.5$ eV and $T = 300$ K, is plotted in Figs. 4(a)–4(c). However, for a real PL measurement, the signal in the high absorption range is limited by noise, which depends on the experimental setup, sample, and measurement conditions. But a 2- to 3-order-of-magnitude difference between the PL peak maximum and the noise level is typically reported [31,35–40]. Thus, random noise is introduced so that the high-energy side of the PL signal can be resolved over intensities spanning 3 orders of magnitude [the blue crosses in Fig. 4(a)]. $\mathcal{R}$ is also computed from the refractive index. When the front and back reflectivity differs, $|r_{j0}|^2$ in Θ_w is replaced by an effective reflectivity r_e which is calculated by solving $\mathcal{R} = r_e[1 + (1 - r_e)^2 X^2/(1 - r_e^2 X^2)]$ with $X = \exp(-\alpha d)$. The computed Θ, Θ_w, and $\Theta_{1-\mathcal{R}}$ values are plotted in Figs. 4(d)–4(f).

The QFLS and the temperature are evaluated from Eq. (14) (where Θ is replaced by Θ_w and $\Theta_{1-\mathcal{R}}$ as appropriate) as previously shown in Fig. 2. The range considered for the evaluation is the range where the absorption is the highest (the high-energy side of the peak) with reliable data, i.e., an acceptable signal-to-noise ratio. The fits are performed on 20 consecutive points within the energy range reported in Figs. 4(g)–4(i). The fitted results are considered valid if the sum of the squared residuals is below 3 times the one obtained for the best fit. The distributions of T and $\Delta\mu$ resulting from valid fits are shown in Figs. 4(g)–4(i). The absorption spectrum is calculated by solving $\Phi^-_{\mathrm{PL}} = \Gamma\Theta_i$, with $\Theta_i = \Theta$, Θ_w, or $\Theta'_{1-\mathcal{R}}$ [leading to Eq. (15) for $\Theta_i = \Theta$], where T and $\Delta\mu$ are taken from the best fit. The resulting absorption spectra are displayed in Figs. 4(j)–4(l).

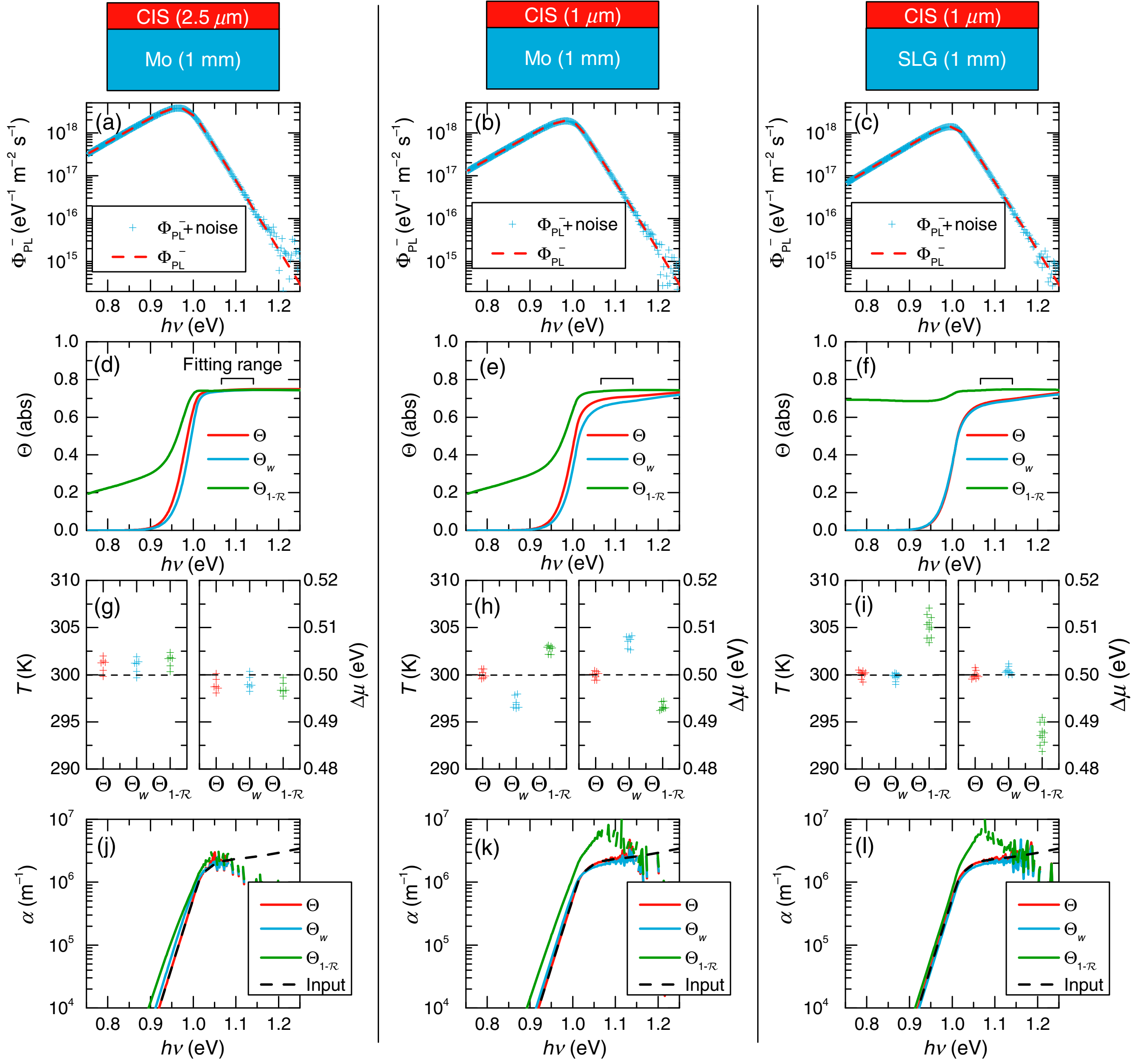

FIG. 4. Simulations comparing the effect of replacing the optical term Θ by its different approximation Θ_w or $\Theta_{1-\mathcal{R}}$ for a $CuInSe_2$ on a Mo or soda-lime glass substrate. (a)–(c) Simulated PL signal for $\Delta\mu = 0.5$ eV and $T = 300$ K. (d)–(f) Comparison of Θ, Θ_w, and $\Theta_{1-\mathcal{R}}$. The fitting range used to retrieve T and $\Delta\mu$ is also indicated. (g)–(i) distribution of retrieved T and $\Delta\mu$. (j)–(l) Comparison of the calculated absorption spectrum.

For the 2.5-μm-thick film on Mo, Θ, Θ_w, and $\Theta_{1-\mathcal{R}}$ have the same value in the energy range used to determine T and $\Delta\mu$, as seen in Fig. 4(d). Accordingly, T and $\Delta\mu$ are satisfactorily evaluated by both Θ approximations [see Fig. 4(g)]. However, in the low absorption range, Θ and Θ_w are different; therefore, the retrieved absorption spectrum using Θ_w does not match the input spectrum. For photon energies below 0.95 eV, the two spectra have nearly the same slope and differ by a factor of 1.5–1.6, giving an error of only 0.3 meV for the Urbach energy. The absorption coefficient measurement using $\Theta_{1-\mathcal{R}}$ yields inaccurate results, with the Urbach energy being overestimated by 1.3 meV.

For thinner CIS like a 1-μm-thick film on Mo, the film is slightly transparent for photons with an energy within the fitting range. The incomplete absorption reduces the PL signal for all energies where $e^{-\alpha d} < 1$ [compare Fig. 4(a) to Fig. 4(b)]. A non-negligible part of the light reflected at the CIS-Mo interface can contribute to the PL signal. Consequently, Θ, Θ_w, and $\Theta_{1-\mathcal{R}}$ are no longer equal in the fitting range [see Fig. 4(e)], leading to inaccurate determinations of T and $\Delta\mu$ [see Fig. 4(h)]. The absorption

spectrum retrieved using Θ_w is 10% lower than the input spectrum near 1.1 eV and is 30%–40% higher for $\hbar\omega < 0.95$ eV, while the Urbach energy is correctly retrieved. The absorption spectrum retrieved using $\Theta_{1-\mathcal{R}}$ is off by at least a factor of 2, and the Urbach energy is overestimated by 1.4 meV.

Replacing the Mo substrate by SLG significantly lowers the back-side reflection. Thus, the front (air and CIS) and back sides (CIS, SLG, and air) have reflection coefficients closer to each other, which makes the wafer approximation more realistic. Indeed, Θ_w is similar to Θ [see Fig. 4(f)], and T and $\Delta\mu$ are correctly evaluated. The absorption spectra have the same shape as the input spectrum and are shifted down by 11%–13%. By contrast, results based on $\Theta_{1-\mathcal{R}}$ are inaccurate, yet the Urbach energy is overestimated by only 0.2–0.3 meV.

The simulation results reported in Fig. 4 show that using the correct optical term Θ is critical for both QFLS and absorption coefficient measurements. As long as the PL signal can be measured reliably in a range where $1 - e^{-\alpha d} \simeq 1$, the wafer approximation Θ_w or rougher approximation $\Theta_{1-\mathcal{R}}$ may be applied to thin films to determine $\Delta\mu$. However, one can also note that the correct determination of $\Delta\mu$ does not imply the correct determination of α. When $\Delta\mu$ is accurate, the absorption coefficient retrieved using Θ_w or $\Theta_{1-\mathcal{R}}$ can be correctly evaluated only in the high absorption range, which is not in the interest of the method. The thickness plays an important role in this consideration, but band tailing is also an important parameter. It is well known that the stronger the band tailing, the stronger the redshift of the PL compared to the band-gap energy [41,42]. Therefore, it is more challenging to measure a reliable PL signal in the high absorption range, where Θ_w or $\Theta_{1-\mathcal{R}}$ may be used to derive $\Delta\mu$ for a semiconductor with strong band tailing. Using the accurate expression in Eq. (13) overcomes those difficulties and also provides an accurate way to extract α, but it requires the knowledge of n for the whole spectral range and of k only in the high-energy range of the PL signal, as demonstrated in Ref. [43].

C. Multiple transition processes

Thus far, we have assumed the transition between an upper (u) and a lower (l) electronic state. The previous derivation holds true for defect states and bands as long as only one quasi-Fermi level can account for the upper-state occupancy and only one quasi-Fermi level can account for the lower-state occupancy. However, it is well known that the PL intensity of shallow transitions and deep transitions scale differently with the laser excitation, ϕ_{laser} [44–46]. For a narrow excitation range, a power law is generally observed: $\Phi^-_{\text{PL}} \propto \phi^p_{\text{laser}}$. For a wide excitation range, however, one should expect a change in p every time a defect level gets saturated due to an increase in photocarrier density. The different exponent p observed for shallow and deep transitions can be calculated from a set of rate transition equations which gives the carrier densities and the occupancies for each level depending on the excitation. One needs additional quasi-Fermi levels to describe the occupancies of the defect states involved in the deeper transitions [47]. When considering more than two quasi-Fermi levels, leading to i recombination processes, Eqs. (1), (2), and (5) are still valid. The individual contribution of the ith transition process is directly derived from those equations by summation over the states involved in this process. However, the photon flux cannot be separated in independent contributions. In that case, the continuity equation takes the form

$$\vec{\nabla} \cdot \vec{\Phi} = \sum_i (R_{\text{sp},i} + R_{\text{sa},i}) = \sum_i (\alpha_i \Gamma_i - \alpha_i \Phi), \qquad (20)$$

which becomes Eq. (8) by substituting $\alpha = \sum_i \alpha_i$ and $\Gamma = \alpha^{-1} \sum_i \alpha_i \Gamma_i$. The PL flux is given by

$$\Phi^-_{\text{PL}} = \alpha^{-1} \sum_i \alpha_i \frac{v_\gamma \rho_\gamma}{\exp(\frac{\hbar\omega - \Delta\mu_i}{k_B T}) - 1} \times \frac{(\mathbb{D} - \frac{\mathbb{B}}{\mathbb{A}}\mathbb{C})(1 - e^{-\alpha d})(1 + \frac{\mathbb{F}}{\mathbb{E}} e^{-\alpha d})}{1 + \frac{\mathbb{F}}{\mathbb{E}}\frac{\mathbb{B}}{\mathbb{A}} e^{-2\alpha d}}, \qquad (21)$$

which reduces to Eq. (13) if the absorption of one process largely prevails over the absorption of the other ($\alpha_i \simeq \alpha$).

We investigate a CGS thin film which shows two contributions to its PL spectrum. As seen in Fig. 5(a), the high-energy peak is attributed to the band-to-band transition (BB), while the low-energy peak is attributed to a transition involving defects (DR). Those two transitions cannot be described by one QFLS, as evidenced by the quite different exponents (p values) of 1.9 for the BB signal and 1.0 for the DR signal.

Close to the band-gap energy, it can be assumed that most of the absorption is due to BB transitions, and the method for the single transition process can be applied. The resulting absorption spectra are plotted in Fig. 5(b). For photon energies above 1.6 eV, the PL signal arises from the BB signal, and the retrieved absorption coefficient corresponds to the band-to-band absorption coefficient. The BB absorption coefficients do not depend on the excitation, even though it is clear from Eqs. (5) and (6) that α depends on the occupation of the upper and lower levels, and thus on QFLS and laser excitation. In the present case, $\hbar\omega - \Delta\mu \gg k_B T$ for $\hbar\omega > 1.6$ eV, and the quasi-Fermi levels are far away from the tail states, $n'_u n_l - n_u n'_l \simeq n'_u n_l$, which is constant in our excitation range. By contrast, the values of the absorption coefficients determined for $\hbar\omega < 1.6$ eV are meaningless since the PL signal arises from DR transitions, but the QFLS used is the one determined for BB transitions. The difficulty in properly determining the absorption coefficient of a DR transition is in the determination of the QFLS because one has to precisely know Θ where the PL signal is due to the DR transition. The absorption for

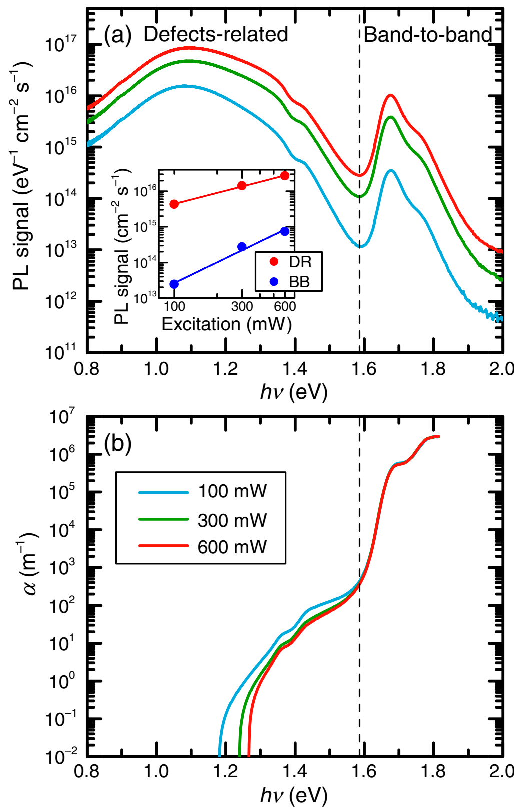

FIG. 5. (a) PL spectra of a CGS thin film under different laser excitations [see the legend of (b)]. (Inset) Log-log plot of the integrated PL signal for the defect-related (DR) signal and the band-to-band (BB) signal. The power-law behavior with $p = 1.0$ for the defect-related transition and $p = 1.9$ for the band-to-band transition. (b) Absorption spectra derived from PL assuming only two quasi-Fermi levels for the whole system.

such an energy range is reduced by several orders of magnitude compared to the absorption at the band-gap energy. In such a low absorption range, it is difficult to reliably measure absorptivity on thin films, which makes it impossible to use PL-based absorption coefficient measurement for defect-related absorption. However, the defect signature is easily detected by PL, which makes it a useful tool to detect and characterize defects in semiconductors. Even for such a complicated case, the band-tail absorption coefficient is correctly resolved over 3 dec, showing the method's worthiness to characterize band-tail absorption.

V. CONCLUSION

In summary, we present in this paper a model based on the transfer-matrix method to extend the measurement of the absorption coefficient and quasi-Fermi level splitting by photoluminescence to multilayer structures. The model is applied on a $CuInSe_2$ thin film deposited on glass. The measured absorption coefficient is in good agreement with photothermal deflection spectroscopy. It is shown that the method used is able to measure absorption coefficients several orders of magnitude lower than SP or PDS, taking advantage of the extreme PL sensitivity to semiconductor absorption. We use the measurement of the absorption coefficient in the energy range of high absorption to extract the QFLS correctly. Once the QFLS is determined, we can then extract from the PL spectrum the absorption spectrum for low absorption values, which is not accessible by other methods.

We give an estimation of the error on the quasi-Fermi-level splitting, the absorption coefficient, and the Urbach energy when applying the model derived for wafers to a thin film deposited on a substrate. If the thin-film absorptivity is large for photon energy corresponding to the high-energy wing of the PL signal (i.e., if the film is thick enough), the quasi-Fermi-level splitting can be measured using an approximated expression of the film absorptivity. However, the general expression derived for multilayers should be used to measure accurately the absorption coefficient.

Finally, we discuss the problematic case of the defect-related transition for which an additional quasi-Fermi-level splitting has to be determined prior to evaluating the absorption coefficient, limiting the present approach. For such a case, the band-tail absorption can be measured, provided that the band-to-band PL signal does not overlap with the defect signal.

ACKNOWLEDGMENTS

This work was funded by Fond National de la Recherche (FNR) under project ODD (Optical detection of deep defects in chalcopyrite semiconductors) (Grant No. C13/MS/5857739). G. Denler, G. Larramona, and S. Bourdais from IMRA are acknowledged for the useful discussions. T. Schuler and P. Ramoa are acknowledged for their assistance.

APPENDIX

For band-to-band transitions, the relation in Eq. (6) can be derived by rewriting the carrier densities, $n_{u,l} = g_{u,l}\rho_{u,l}f_{u,l}$ and $n'_{u,l} = g_{u,l}\rho_{u,l}f'_{u,l}$, with $f_{u,l} = [\exp(E_{u,l} - F_{u,l}/k_BT) + 1]^{-1}$, F being the Fermi level, and $f' = 1 - f$:

$$\frac{n_u n'_l}{n'_u n_l - n_u n'_l} = \frac{f_u f'_l}{f'_u f_l - f_u f'_l} = \frac{f_u f'_l}{f_l - f_u} = \frac{1}{\exp\left(\frac{\hbar\omega - \Delta\mu}{k_BT}\right) - 1}. \tag{A1}$$

The last step is done by identifying $E_u - E_l = \hbar\omega$ and $\Delta\mu = F_u - F_l$. For a monovalent acceptor, $n_a = g_a N_a f_a$ and $n'_a = N_a f'_a$, with $f_a = [g_a \exp(E_a - F_a/k_BT) + 1]^{-1}$ and $f'_a = 1 - f_a = g_a[g_a + \exp(F_a - E_a/k_BT)]^{-1}$, which leads to the same results [18].

The error bars shown in Fig. 3 are calculated by rewriting Eq. (15) as

$$\alpha = -\frac{1}{d}\ln\left(\frac{(r_1-1)+\chi}{2(r_1+\frac{r_2}{r_0}\Phi_{PL}^{-}/\Gamma)}\right), \qquad (A2)$$

where

$$\chi = \sqrt{(r_1-1)^2+4\left(r_1+\frac{r_2}{r_0}\Phi_{PL}^{-}/\Gamma\right)\left(1-\frac{1}{r_0}\Phi_{PL}^{-}/\Gamma\right)},$$

with $r_0 = \mathbb{D} - (\mathbb{B}/\mathbb{A})\mathbb{C}$, $r_1 = (\mathbb{F}/\mathbb{E})$, and $r_2 = (\mathbb{F}/\mathbb{E})\times(\mathbb{B}/\mathbb{A})$. The uncertainty on α is then estimated as

$$\delta\alpha = \frac{\partial\alpha}{\partial d}\delta d + \frac{\partial\alpha}{\partial r_0}\delta r_0 + \frac{\partial\alpha}{\partial r_1}\delta r_1 + \frac{\partial\alpha}{\partial r_2}\delta r_2 + \delta(\Phi_{PL}^{-}/\Gamma). \qquad (A3)$$

As the set of equations in Eq. (16) does not allow us to explicitly write r_0, r_1, or r_2 as a function of the experimental parameters, their respective uncertainties δr_0, δr_1, and δr_2 are calculated by numerically propagating the uncertainty. The parameters $\mathcal{T}$, $\mathcal{R}$, and d and the wavelength λ are simultaneously adjusted within their error interval ($\delta\mathcal{T} = \pm 0.01$, $\delta\mathcal{R} = \pm 0.02$, $\delta d = \pm 10$ nm, and $\delta\lambda = \pm 0.3$ nm) in order to produce the maximal deviation of r_0, r_1, or r_2.

$\delta(\Phi_{PL}^{-}/\Gamma)$ is the α uncertainty due to the error on Φ_{PL}^{-}/Γ. The Γ error is calculated by using Eq. (14). The right-hand term is affected by $\delta\Phi_{PL}^{-} = \pm 0.01\Phi_{PL}^{-} \pm 2\times 10^{11}\ \mathrm{eV^{-1}\,cm^{-2}\,s^{-1}}$ and $\delta\Theta$, which is evaluated in the same way as δr_0. Then the left-hand term is determined with a linear fitting. The fitting errors are estimated by bootstrap resampling. The energy range for the fitting is randomly chosen among the ranges that give low residuals, then the selected data points are randomly varied within their uncertainty interval resulting from $\delta\Phi_{PL}^{-}$ and $\delta\Theta$ and the fit is applied to this modified data set. The process is repeated 1000 times in order to produce significant statistics and enable us to determine the maximum variation of Γ. $\delta\Gamma$ and $\delta\Phi_{PL}^{-}$ are injected into Eq. (A2) to determine $\delta(\Phi_{PL}^{-}/\Gamma)$.

---

[1] Piet Van Mieghem, Theory of band tails in heavily doped semiconductors, Rev. Mod. Phys. **64**, 755 (1992).

[2] Sungsik Lee, Khashayar Ghaffarzadeh, Arokia Nathan, John Robertson, Sanghun Jeon, Changjung Kim, I-Hun Song, and U-In Chung, Trap-limited and percolation conduction mechanisms in amorphous oxide semiconductor thin film transistors, Appl. Phys. Lett. **98**, 203508 (2011).

[3] R. Martins, P. Barquinha, I. Ferreira, L. Pereira, G. Gonalves, and E. Fortunato, Role of order and disorder on the electronic performances of oxide semiconductor thin film transistors, J. Appl. Phys. **101**, 044505 (2007).

[4] William Shockley and Hans J. Queisser, Detailed balance limit of efficiency of *p-n* junction solar cells, J. Appl. Phys. **32**, 510 (1961).

[5] U. Rau and J. H. Werner, Radiative efficiency limits of solar cells with lateral band-gap fluctuations, Appl. Phys. Lett. **84**, 3735 (2004).

[6] T. Tiedje, Band tail recombination limit to the output voltage of amorphous silicon solar cells, Appl. Phys. Lett. **40**, 627 (1982).

[7] Stefaan De Wolf, Jakub Holovsky, Soo-Jin Moon, Philipp Lper, Bjoern Niesen, Martin Ledinsky, Franz-Josef Haug, Jun-Ho Yum, and Christophe Ballif, Organometallic halide perovskites: Sharp optical absorption edge and its relation to photovoltaic performance, J. Phys. Chem. Lett. **5**, 1035 (2014).

[8] Jasmin J. Thevaril and Stephen K. O'Leary, The role that conduction band tail states play in determining the optical response of hydrogenated amorphous silicon, Solid State Commun. **151**, 730 (2011).

[9] Franz Urbach, The long-wavelength edge of photographic sensitivity and of the electronic absorption of solids, Phys. Rev. **92**, 1324 (1953).

[10] D. L. Dexter, Interpretation of Urbach's rule, Phys. Rev. Lett. **19**, 1383 (1967).

[11] John D. Dow and David Redfield, Toward a unified theory of Urbach's rule and exponential absorption edges, Phys. Rev. B **5**, 594 (1972).

[12] C. M. Soukoulis, M. H. Cohen, and E. N. Economou, Exponential Band Tails in Random Systems, Phys. Rev. Lett. **53**, 616 (1984).

[13] Sajeev John, Costas Soukoulis, Morrel H. Cohen, and E. N. Economou, Theory of Electron Band Tails and the Urbach Optical-Absorption Edge, Phys. Rev. Lett. **57**, 1777 (1986).

[14] C. W. Greeff and H. R. Glyde, Anomalous Urbach tail in GaAs, Phys. Rev. B **51**, 1778 (1995).

[15] David Redfield, Energy-band tails and the optical absorption edge; The case of *a*-Si:H, Solid State Commun. **44**, 1347 (1982).

[16] John K. Katahara and Hugh W. Hillhouse, Quasi-Fermi level splitting and sub-bandgap absorptivity from semiconductor photoluminescence, J. Appl. Phys. **116**, 173504 (2014).

[17] E. Daub and P. Würfel, Ultralow Values of the Absorption Coefficient of Si Obtained from Luminescence, Phys. Rev. Lett. **74**, 1020 (1995).

[18] H. Barry Bebb and E. W. Willams, in *Transport and Optical Phenomena*, edited by R. W. Willardson and Albert C. Beer, Semiconductors and Semimetals Vol. 8 (Academic Press, New York, 1972).

[19] W. van Roosbroeck and W. Shockley, Photon-radiative recombination of electrons and holes in germanium, Phys. Rev. **94**, 1558 (1954).

[20] Gordon Lasher and Frank Stern, Spontaneous and stimulated recombination radiation in semiconductors, Phys. Rev. **133**, A553 (1964).

[21] R. Carius, F. Becker, H. Wagner, and J.-Th. Zettler, Electroluminescence and transport in *a*-Si:H *p-i-n* diodes at room temperature, Mater. Res. Soc. Symp. Proc. **297**, 357 (1993).

[22] S. Knabe, M. Langemeyer, F. Heidemann, R. Brggemann, and G. H. Bauer, Study of the effect of excess carrier lifetime depth profiles and depth dependent absorption coefficients on the emitted photoluminescence spectrum

of chalcopyrite thin films, Prog. Photovoltaics **19**, 927 (2011).

[23] Charalambos C. Katsidis and Dimitrios I. Siapkas, General transfer-matrix method for optical multilayer systems with coherent, partially coherent, and incoherent interference, Appl. Opt. **41**, 3978 (2002).

[24] K. Schick, E. Daub, S. Finkbeiner, and P. Würfel, Verification of a generalized Planck law for luminescence radiation from silicon solar cells, Appl. Phys. A **54**, 109 (1992).

[25] T. Trupke, E. Daub, and P. Würfel, Absorptivity of silicon solar cells obtained from luminescence, Sol. Energy Mater. Sol. Cells **53**, 103 (1998).

[26] Thomas Unold and Levent Gütay, Photoluminescence analysis of thin-film solar cells, in *Advanced Characterization Techniques for Thin Film Solar Cells*, edited by Daniel Abou-Ras, Thomas Kirchartz, and Uwe Rau, Vol. 1 (Wiley-VCH, Weinheim, 2011), Chap. 7, pp. 151–175.

[27] W. B. Jackson, N. M. Amer, A. C. Boccara, and D. Fournier, Photothermal deflection spectroscopy and detection, Appl. Opt. **20**, 1333 (1981).

[28] Susanne Siebentritt, Levent Gütay, David Regesch, Yasuhiro Aida, and Valérie Deprédurand, Why do we make $Cu(In,Ga)Se_2$ solar cells non-stoichiometric?, Sol. Energy Mater. Sol. Cells **119**, 18 (2013).

[29] L. Gütay and G. H. Bauer, Local fluctuations of absorber properties of $Cu(In,Ga)Se_2$ by sub-micron resolved PL towards "real life" conditions, Thin Solid Films **517**, 2222 (2009).

[30] Hendrik Sträter, Sebastian ten Haaf, Rudolf Brüggemann, Gerhard Jakob, Niklas Nilius, and Gottfried H. Bauer, Detailed photoluminescence study of vapor deposited Bi_2S_3 films of different surface morphology, Phys. Status Solidi (b) **251**, 2247 (2014).

[31] Finn Babbe, Leo Choubrac, and Susanne Siebentritt, Quasi Fermi level splitting of Cu-rich and Cu-poor $Cu(In,Ga)Se_2$ absorber layers, Appl. Phys. Lett. **109**, 082105 (2016).

[32] Philip Jackson, Roland Wuerz, Dimitrios Hariskos, Erwin Lotter, Wolfram Witte, and Michael Powalla, Effects of heavy alkali elements in $Cu(In,Ga)Se_2$ solar cells with efficiencies up to 22.6%, Phys. Status Solidi RRL **10**, 583 (2016).

[33] Sopra SA database, http://www.sspectra.com/sopra.html.

[34] P. D. Paulson, R. W. Birkmire, and W. N. Shafarman, Optical characterization of $CuIn_{1-x}Ga_xSe_2$ alloy thin films by spectroscopic ellipsometry, J. Appl. Phys. **94**, 879 (2003).

[35] Amaury Delamarre, Myriam Paire, Jean-Francois Guillemoles, and Laurent Lombez, Quantitative luminescence mapping of $Cu(In,Ga)Se_2$ thin-film solar cells, Prog. Photovoltaics **23**, 1305 (2015).

[36] Amaury Delamarre, Laurent Lombez, and Jean-Francois Guillemoles, Contactless mapping of saturation currents of solar cells by photoluminescence, Appl. Phys. Lett. **100**, 131108 (2012).

[37] F. Heidemann, R. Brüggemann, and G. H. Bauer, The correlation between local defect absorbance and quasi-Fermi level splitting in $CuInS_2$ from photoluminescence, J. Phys. D **43**, 145103 (2010).

[38] H. Sträter, R. Brüggemann, S. Siol, A. Klein, W. Jaegermann, and G. H. Bauer, Detailed photoluminescence studies of thin film Cu_2S for determination of quasi-Fermi level splitting and defect levels, J. Appl. Phys. **114**, 233506 (2013).

[39] L. Gütay and G. H. Bauer, Lateral variations of optoelectronic quality of $Cu(In_{1-x}Ga_x)Se_2$ in the submicron-scale, Thin Solid Films **487**, 8 (2005).

[40] G. H. Bauer, R. Brüggemann, S. Tardon, S. Vignoli, and R. Kniese, Quasi-Fermi level splitting and identification of recombination losses from room temperature luminescence in $Cu(In_{1-x}Ga_x)Se_2$ thin films versus optical band gap, Thin Solid Films **480–481**, 410 (2005).

[41] Tayfun Gokmen, Oki Gunawan, Teodor K. Todorov, and David B. Mitzi, Band tailing and efficiency limitation in kesterite solar cells, Appl. Phys. Lett. **103**, 103506 (2013).

[42] Susanne Siebentritt, Why are kesterite solar cells not 20% efficient?, Thin Solid Films **535**, 1 (2013).

[43] G. Rey, G. Larramona, S. Bourdais, C. Chone, B. Delatouche, A. Jacob, G. Dennler, and S. Siebentritt, On the origin of band-tails in kesterite (to be published).

[44] T. Schmidt, K. Lischka, and W. Zulehner, Excitation-power dependence of the near-band-edge photoluminescence of semiconductors, Phys. Rev. B **45**, 8989 (1992).

[45] W. Grieshaber, E. F. Schubert, I. D. Goepfert, R. F. Karlicek, M. J. Schurman, and C. Tran, Competition between band gap and yellow luminescence in GaN and its relevance for optoelectronic devices, J. Appl. Phys. **80**, 4615 (1996).

[46] C. Spindler, G. Rey, and S. Siebentritt, Excitation dependence of shallow and deep-level photoluminescence transitions (to be published).

[47] Peter Wurfel, Improvement of solar cell efficiencies by impurity transitions, Sol. Energy Mater. Sol. Cells **79**, 153 (2003).